Pergamon

Int. J. Heat Mass Transfer. Vol. 41, No. 1, pp. 159–174, 1998

Printed in Great Britain
0017-9310/98 $19.00+0.00

PII: S0017-9310(97)00075-6

Vapor and liquid flow in an asymmetrical flat plate heat pipe: a three-dimensional analytical and numerical investigation

N. ZHU and K. VAFAI†

Department of Mechanical Engineering, The Ohio State University, Columbus, OH 43210, U.S.A.

(*Received* 26 *November* 1996 *and in final form* 15 *February* 1997)

Abstract—In this work, an analytical and numerical study was carried out for the steady incompressible vapor and liquid flow in an asymmetrical flat plate heat pipe. The pseudo-three-dimensional analytical model employs the boundary layer approximation to describe the vapor flow under conditions including strong flow reversal and the method of matched asymptotic expansions to incorporate the non-Darcian effects for the liquid flow through the porous wicks. The coupling of the liquid flow in the top, bottom and vertical wicks is also included in the model. In the numerical study, a finite element scheme based on the Galerkin method of weighted residuals was used to solve the full set of nonlinear differential elliptical equations of motion and the continuity equation for the three-dimensional vapor flow. The analytical and numerical results for various injection Reynolds numbers are presented. The three-dimensional effects are discussed and the results show that a three-dimensional analysis is necessary if the vapor channel width-to-height ratio is less than 2.5. Very good agreement was found between the analytical and the numerical results. While showing, qualitatively and quantitatively, the pertinence and the effects of various physical parameters, the analytical results are quite useful for practical engineering purposes by providing an effective and rapid prediction method for the flat plate heat pipe operation. © 1997 Elsevier Science Ltd.

INTRODUCTION

Heat pipes have been widely used in heat transfer related application in the last three decades. Research data on conventional cylindrical heat pipes, both theoretical and experimental, have been well-established for various applications. Asymmetrical heat pipes, either flat plate [1–4] or disk-shaped [5–7], have applications in electronic cooling, spacecraft thermal control and commercial thermal devices. These applications require an understanding of the behavior and performance of the flat plate and disk-shaped heat pipes with asymmetrical heat inputs. In general, the analytical and numerical analysis developed for conventional cylindrical heat pipes cannot be applied to asymmetrical heat pipes.

Only a few investigators have studied the vapor and liquid flow in asymmetrical flat plate heat pipes, which is a more complicated and less understood system compared to conventional cylindrical heat pipes. Ooijen and Hoogendoorn [3] carried out a two-dimensional numerical investigation for steady incompressible laminar vapor flow in a flat plate heat pipe with an adiabatic top plate. They solved the vapor mass and momentum equations using the control volume finite difference approach for the injection (radial) Reynolds number over the range of $1 \leqslant Re_r \leqslant 50$. Their results show that, the velocity profiles are non-similar and asymmetrical for injection (radial) Reynolds number $Re_r > 1$. Flow reversal is encountered in the condenser section at $Re_r > 10$.

Vafai and Wang [4] have proposed an asymmetrical flat plate heat pipe design. In their design the vapor space is divided into several channels by vertical wicks. For the heat pipes heated from the top surface, this is quite advantageous for the condensate return thus enhancing the heat pipe performance. They had developed a pseudo-three-dimensional analytical model for incompressible vapor and liquid flow within the flat plate heat pipe. In their study, the vapor flow field was bifurcated on the x–y plane due to the asymmetrical feature of heat input. The parabolic velocity profiles, which vary with the distance along the heat pipe, were used for both upper and lower parts of vapor flow within the heat pipe. The liquid flow was modeled by using Darcy's law with the assumption of the same liquid flow rates in the top and bottom wicks.

Vafai *et al.* [6] have analyzed the asymmetrical disk-shaped heat pipes and developed a comprehensive analytical model for it. The generalized momentum equation in porous medium was employed to describe the liquid flow in the disk-shaped heat pipe. The coupling of the liquid flow within the top and bottom wicks was established and the vapor–liquid coupling and the gravitational effects were also accounted for in the analytical model for the disk-shaped heat pipe [7]. This model was used to simulate the disk-shaped heat pipe tested by North and Avedisian [5] and good agreement was found between the predicted maximum

† Author to whom correspondence should be addressed.

NOMENCLATURE

A_1, A_2, A_3 coefficient defined by equations (31)–(33)
a_3 coefficient used in the vapor velocity profile for the $0 < y^+ < f^+$ region
B_1, B_2 coefficient defined by equations (34) and (35)
b_3 coefficient used in the vapor velocity profile for the $f^+ < y^+ < 1$ region
D_2 constant defined by equation (36)
Da Darcy number of porous wicks defined as $K/\varepsilon h^2$
f location of the maximum vapor velocity [m]
g gravitational acceleration
h vapor channel height [m]
h_w top and bottom wick thickness [m]
h_{vw} vertical wick thickness [m]
K permeability of porous wicks [m^2]
L length of the flat plate heat pipe [m]
L_e length of the evaporation zone [m]
p pressure [Pa]
Re_h injection Reynolds number, $\rho_v v_1 h/\mu_v$
u, v, w velocity components in the x^+, y^+ and z^+ direction, respectively, [m s^{-1}]
U the maximum axial velocity component [m s^{-1}]
u_1 characteristics value for radial velocity component, $v_1 L/h$
v_1 vapor injection velocity [m s^{-1}]
v_2 vapor suction velocity [m s^{-1}]
W width of vapor flow channel [m]
x, y, z coordinates [m].

Greek symbols
α ratio of half of the vapor channel width to its height, $W/2h$
β ratio of the vapor channel length to its height, L/h
ε porosity of the porous wicks
φ ratio of the evaporator length to the heat pipe length, L_e/L
μ dynamic viscosity [N s m^{-2}]
ρ density [kg m^{-3}].

Subscripts
b bottom wick
l liquid phase
t top wick
v vapor phase
vw vertical wick
w top and bottom wicks.

Superscript
+ dimensionless quantity.

heat transfer and the measured data. The model was further extended to vapor flow predictions in the presence of flow reversal [8]. In this work, Zhu and Vafai [8] also studied the three-dimensional vapor flow in the disk-shaped heat pipe numerically. In their study, the nonlinear differential elliptical equations of motion were solved over the entire vapor flow channel in order to allow all of the features of the incompressible vapor flow to be taken into account. The comparison of their analytical and numerical results further demonstrated that the analytical model predicts the velocity variation and pressure drop accurately along the disk-shaped heat pipe.

In the present study, the analytical model developed by Vafai and Wang [4] is extended to account for the vapor flow reversals, the liquid flow in the vertical wicks, the coupling of the liquid flow within the top and bottom wicks, the non-Darcian effects of the liquid flow though the porous wicks and the gravitational effects. In addition, the complete three-dimensional vapor flow in the flat plate heat pipe is analyzed numerically for the first time. The analytical results are compared with the numerical results and are found to be in good agreement. It is worth noting that the analytical model reduces the computational time drastically by several orders of magnitude.

MATHEMATICAL MODELING

The physical problem under consideration is a horizontal flat plate heat pipe, as shown in Fig. 1. Heat is input from the top center surface of the heat pipe, so that the flow and heat transfer become asymmetrical. The vapor space is divided into several channels by the vertical wicks which transport liquid from the bottom wick to the top wick. Any one of the internal channels can be considered as a building block for the flat plate heat pipe. Once the fluid flow characteristics within one of the channels is determined, the fluid flow characteristics of the entire heat pipe can be easily established. The results of this analysis are applicable to any number of channels.

Steady, incompressible, three-dimensional laminar vapor and liquid flow in a channel is considered, as shown in Fig. 1(b). All wicks are assumed to be isotropic and saturated with wetting liquid. The transport properties of the fluid are assumed to be constant. The vapor injection and suction rates are assumed to

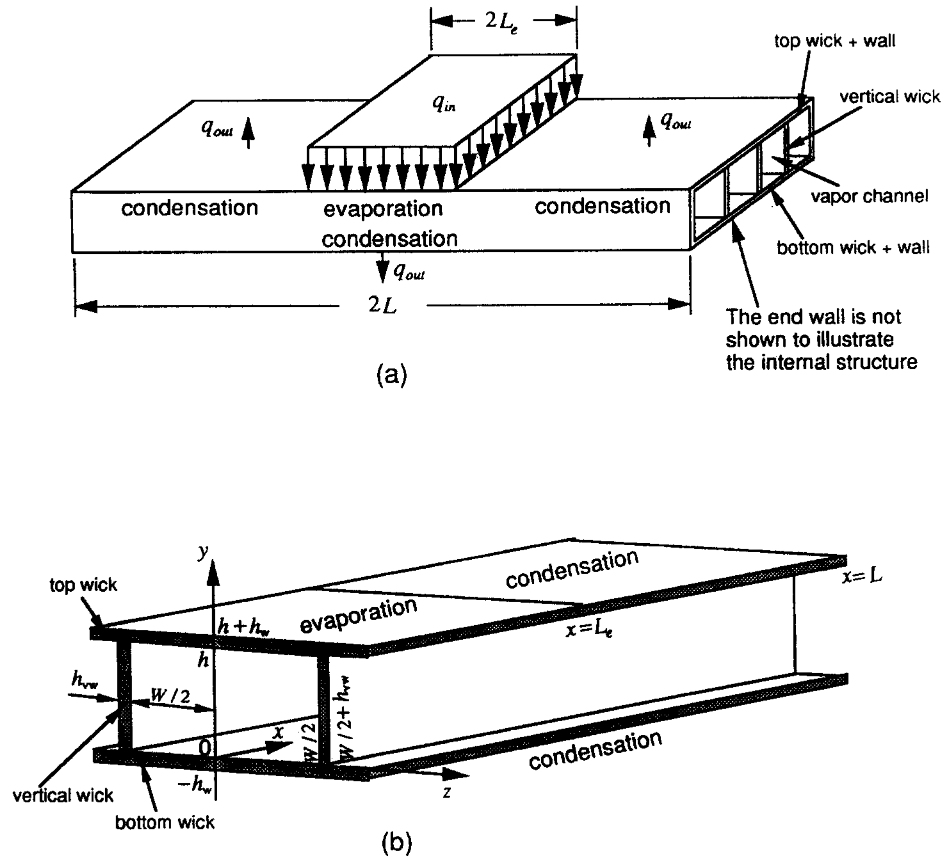

Fig. 1. Schematic of the flat plate heat pipe: (a) configuration of the heat pipe; (b) the wick structure and the coordinate system within a channel.

be uniform on the top and bottom wicks and negligible on the vertical wicks. The differential equations associated with this three-dimensional problem are the continuity and the momentum equations. The mathematical model of the vapor and liquid flow within a channel is described by four subregions: the vapor region, the top liquid–wick region, the bottom liquid–wick region and the vertical liquid–wick region, each of which has its own set of governing equations. In the vapor region, the continuity and momentum equations are:

$$\frac{\partial u_v}{\partial x}+\frac{\partial v_v}{\partial y}+\frac{\partial w_v}{\partial z}=0 \tag{1}$$

$$\rho_v\left(u_v\frac{\partial u_v}{\partial x}+v_v\frac{\partial u_v}{\partial y}+w_v\frac{\partial u_v}{\partial z}\right)=-\frac{\partial p_v}{\partial x}+\mu_v\left(\frac{\partial^2 u_v}{\partial x^2}+\frac{\partial^2 u_v}{\partial y^2}+\frac{\partial^2 u_v}{\partial z^2}\right) \tag{2}$$

$$\rho_v\left(u_v\frac{\partial v_v}{\partial x}+v_v\frac{\partial v_v}{\partial y}+w_v\frac{\partial v_v}{\partial z}\right)=-\frac{\partial p_v}{\partial y}+\mu_v\left(\frac{\partial^2 v_v}{\partial x^2}+\frac{\partial^2 v_v}{\partial y^2}+\frac{\partial^2 v_v}{\partial z^2}\right) \tag{3}$$

$$\rho_v\left(u_v\frac{\partial w_v}{\partial x}+v_v\frac{\partial w_v}{\partial y}+w_v\frac{\partial w_v}{\partial z}\right)=-\frac{\partial p_v}{\partial z}+\mu_v\left(\frac{\partial^2 w_v}{\partial x^2}+\frac{\partial^2 w_v}{\partial y^2}+\frac{\partial^2 w_v}{\partial z^2}\right). \tag{4}$$

The equation of motions for the liquid flow within the top and bottom wicks are based on the generalized momentum equation [9, 10] which accounts for the boundary and inertial effects. The convective term in the generalized momentum equation is dropped in accordance with the work of Vafai and Tien [9, 10]. The governing equations for the liquid flow in the top wick are:

$$\frac{\partial u_{l,t}}{\partial x}+\frac{\partial v_{l,t}}{\partial y}+\frac{\partial w_{l,t}}{\partial z}=0 \tag{5}$$

$$\frac{\mu_l}{\varepsilon_w}\left(\frac{\partial^2 u_{l,t}}{\partial x^2}+\frac{\partial^2 u_{l,t}}{\partial y^2}+\frac{\partial^2 u_{l,t}}{\partial z^2}\right)-\frac{\mu_l}{K_w}u_{l,t}-\frac{\rho_l F\varepsilon_w}{K_w^{1/2}}|u_{l,t}|u_{l,t}-\frac{\partial p_{l,t}}{\partial x}=0 \tag{6}$$

and for the liquid flow in the bottom wick are

$$\frac{\partial u_{l,b}}{\partial x}+\frac{\partial v_{l,b}}{\partial y}+\frac{\partial w_{l,b}}{\partial z}=0 \tag{7}$$

$$\frac{\mu_l}{\varepsilon_w}\left(\frac{\partial^2 u_{l,b}}{\partial x^2}+\frac{\partial^2 u_{l,b}}{\partial y^2}+\frac{\partial^2 u_{l,b}}{\partial z^2}\right)-\frac{\mu_l}{K_w}u_{l,b} - \frac{\rho_l F\varepsilon_w}{K_w^{1/2}}|u_{l,b}|u_{l,b}-\frac{\partial p_{l,b}}{\partial x}=0. \quad (8)$$

The liquid flow within the top and bottom wicks are coupled through the liquid flow within the vertical wicks. Since the heat is removed from the top and bottom surfaces of the heat pipe and there is no heat sink to remove heat from the vertical wicks directly, the main role of the vertical wicks is to transport liquid from the bottom wick to the top wick. Based on these considerations, vapor injection and suction on the vertical wicks as well as the axial liquid flow within the vertical wicks are negligible. Therefore, the mass conservation for the liquid within the vertical wicks yields:

$$Q_b(x)=Q_t(x)=Q(x) \quad (9)$$

where

$$Q_b(x)=\int_{-h_w}^{0}(w_{l,b}(x,y,z=W/2) - w_{l,b}(x,y,z=-W/2))\,dy \quad (10)$$

is the flow rate of liquid from the bottom wick to the vertical wicks at location x and

$$Q_t(x)=-\int_{h}^{h+h_w}(w_{l,t}(x,y,z=W/2) - w_{l,b}(x,y,z=-W/2))\,dy \quad (11)$$

is the flow rate of liquid from the vertical wicks to the top wick at location x. For the horizontal heat pipe under study, the liquid flow within the vertical wicks is described by using Darcy's law, that is:

$$Q(x)=-\frac{K_{vw}h_{vw}}{\mu_l}\left(\frac{p_{l,t}(x)-p_{l,b}(x)}{h}+\rho_l g\right). \quad (12)$$

The boundary conditions are:

$$x=0:\quad u_v=v_v=w_v=u_{l,b}=u_{l,t}=0$$
$$x=L:\quad u_v=v_v=w_v=u_{l,b}=u_{l,t}=0,\quad p_v=p_{l,b}$$
$$z=-W/2:\quad u_v=v_v=w_v=u_{l,b}=u_{l,t}=0$$
$$z=W/2:\quad u_v=v_v=w_v=u_{l,b}=u_{l,t}=0$$
$$y=-h_w:\quad u_{l,b}=v_{l,b}=w_{l,b}=0$$
$$y=0:\quad u_v=w_v=u_{l,b}=w_{l,b}=0,\quad \rho_v v_v=\rho_l v_{l,b}=-\rho_v v_2$$
$$y=h:\quad u_v=w_v=u_{l,b}=w_{l,b}=0,\quad \rho_v v_v=\rho_l v_{l,t}=\begin{cases}-\rho_v v_1 & (0\leqslant x\leqslant \varphi L)\\ \rho_v v_2 & (\varphi L\leqslant x\leqslant L)\end{cases}$$
$$y=h+h_w:\quad u_{l,t}=v_{l,t}=w_{l,t}=0$$
$$p_v(0,y,z)=0 \quad (13)$$

where the last condition assigns the reference point for the vapor pressure. The vapor injection velocity v_1 is related to the input power Q_{in} by the following relation:

$$v_1=\frac{Q_{in}}{2\rho_v h_{fg}L_e W} \quad (14)$$

where h_{fg} is the latent heat of the working fluid. The vapor suction velocity v_2 is obtained by the mass balance which requires that the fluid that entering the vapor channel in the evaporator section to flow out through the condenser section. It should be noted that the interfacial coupling is negligible, based on the analysis presented in Zhu and Vafai [7].

ANALYTICAL SOLUTION

Vapor flow

Based on physical considerations, the vapor injection/suction on the vertical wicks is negligible. Therefore, the z component of the vapor velocity is negligible and the governing equations (1)–(4) in the dimensionless variables:

$$x^+=\frac{x}{L},\quad y^+=\frac{y}{h},\quad z^+=\frac{z}{W/2},$$
$$u_v^+=\frac{u_v}{u_1},\quad v_v^+=\frac{V_v}{V_1},\quad p_v^+=\frac{p_v}{\rho_v u_1^2} \quad (15)$$

reduces to the form

$$\frac{\partial u_v^+}{\partial x^+}+\frac{\partial v_v^+}{\partial y^+}=0 \quad (16)$$

$$u_v^+\frac{\partial u_v^+}{\partial x^+}+v_v^+\frac{\partial u_v^+}{\partial y^+}=-\frac{\partial p_v^+}{\partial x^+}+\frac{Re_h}{Re_1^2}\frac{\partial^2 u_v^+}{\partial (x^+)^2} + \frac{1}{Re_h}\left(\frac{\partial^2 u_v^+}{\partial (y^+)^2}+\frac{1}{\alpha^2}\frac{\partial^2 u_v^+}{\partial (z^+)^2}\right) \quad (17)$$

$$\frac{Re_h^2}{Re_1^2}\left(u_v^+\frac{\partial v_v^+}{\partial x^+}+v_v^+\frac{\partial v_v^+}{\partial y^+}\right)=-\frac{\partial p_v^+}{\partial y^+}+\frac{Re_h^3}{Re_1^4}\frac{\partial^2 v_v^+}{\partial (x^+)^2} + \frac{Re_h}{Re_1^2}\left(\frac{\partial^2 v_v^+}{\partial (y^+)^2}+\frac{1}{\alpha^2}\frac{\partial^2 v_v^+}{\partial (z^+)^2}\right) \quad (18)$$

$$\frac{\partial p_v^+}{\partial z^+}=0 \quad (19)$$

where

$$u_1=\frac{L}{h}v_1,\quad Re_h=\frac{\rho_v v_1 h}{\mu_v},$$
$$Re_1=\frac{\rho_v u_1 h}{\mu_v},\quad \alpha=\frac{W/2}{h}.$$

To obtain an analytical solution for the asymmetrical flat plate heat pipe, we note that the heat pipe is long enough such that the vapor injection Reynolds number Re_h is small with respect to Re_1. We also note that the width of each vapor channel is of the same magnitude as its height. In this case, which covers most practical situations, equations (17)–(19) reduce to the form:

$$u_v^+ \frac{\partial u_v^+}{\partial x^+} + v_v^+ \frac{\partial u_v^+}{\partial y^+} = -\frac{\partial p_v^+}{\partial x^+} + \frac{1}{Re_h}\left(\frac{\partial^2 u_v^+}{\partial (y^+)^2} + \frac{1}{\alpha^2}\frac{\partial^2 u_v^+}{\partial (z^+)^2}\right) \tag{20}$$

$$\frac{\partial p_v^+}{\partial y^+} = 0 \tag{21}$$

$$\frac{\partial p_v^+}{\partial z^+} = 0. \tag{22}$$

This indicates that the vapor flow in a long flat plate heat pipe can be calculated on the basis of the simpler system of equations for a boundary layer. The validity of the boundary layer approximation was examined by Busse and Prenger [11], where good agreement was obtained between the pressure distributions along a cylindrical condenser predicted by using the boundary layer equations and those obtained using the Navier–Stokes equations for the ratio of the condenser length to its diameter as small as 2.5. The two-dimensional numerical study by Ooijen and Hoogendoorn [3] also revealed negligible transverse pressure difference in the y-direction for the vapor flow in an asymmetrical flat plate heat pipe.

The boundary conditions in the dimensionless form reduce to:

$$u_v^+(0,y^+,z^+) = v_v^+(0,y^+,z^+) = u_v^+(1,y^+,z^+) = v_v^+(1,y^+,z^+) = 0$$

$$u_v^+(x^+,0,z^+) = u_v^+(x^+,1,z^+) = 0$$

$$v_v^+(x^+,0,z^+) = -v_2^+$$

$$v_v^+(x^+,1,z^+) = \begin{cases} -1, & 0 \leqslant x^+ \leqslant \varphi \\ v_2^+, & \varphi \leqslant x^+ \leqslant 1 \end{cases}$$

$$u_v^+(x^+,y^+,-1) = v_v^+(x^+,y^+,-1) = u_v^+(x^+,y^+,1) = v_v^+(x^+,y^+,1) = 0$$

$$p_v^+(0,y^+,z^+) = 0. \tag{23}$$

For the analytical solution, the velocity profile is approximated by a functional product in the x^+-, y^+-, z^+-directions:

$$u_v^+(x^+,y^+,z^+) = U_v^+(x^+)(a_0(x^+) + a_1(x^+)y^+ + a_2(x^+)(y^+)^2 + a_3(x^+)(y^+)^3)(c_0 + c_1 z^+ + c_2(z^+)^2) \tag{24}$$

where $U_v^+(x^+)$ denotes the maximum axial velocity component on each transverse surface along the x^+-direction. A third-order polynomial is used in equation (24) to account for the flow reversal in the x^+–y^+-plane. Due to the vapor injection from the heating side of the top wick, the location of maximum vapor velocity $U_v^+(x^+)$ will be shifted towards the bottom wick within the $0 \leqslant x^+ \leqslant \varphi$ region. As the vapor flows downstream, the location of $U_v^+(x^+)$ will gradually shift towards the center in the y^+-direction due to the presence of symmetrical cooling conditions. To account for this feature, the vapor velocity profile in the y^+-direction is divided into two parts based on the location of the maximum vapor velocity: the lower part $(0 \leqslant y^+ \leqslant f^+(x^+))$ and the upper part $(f^+(x^+) \leqslant y^+ \leqslant 1)$. The location of maximum vapor velocity, $y^+ = f^+(x^+)$, is also the location corresponding to zero shear stress for the velocity distribution in the x^+–y^+ plane. Applying the boundary conditions given in equation (23) and

$$u_v^+(x^+, f^+(x^+), 0) = U_v^+(x^+), \quad \left.\frac{\partial u_v^+}{\partial y^+}\right|_{y^+ = f^+(x^+)} = 0 \tag{25}$$

to equation (24) results in the following velocity profile:

$$u_v^+(x^+,y^+,z^+) = \begin{cases} U_v^+(x^+)\left\{a_3(x^+)\frac{y^+}{f^+} + \left(1 - a_3(x^+)\frac{y^+}{f^+}\right) \times \left[2\frac{y^+}{f^+} - \left(\frac{y^+}{f^+}\right)^2\right]\right\}(1-(z^+)^2) \\ (0 \leqslant y^+ \leqslant f^+(x^+)) \\ U_v^+(x^+)\left\{b_3(x^+)\frac{1-y^+}{1-f^+} + \left(1 - b_3(x^+)\frac{1-y^+}{1-f^+}\right) \times \left[2\frac{1-y^+}{1-f^+} - \left(\frac{1-y^+}{1-f^+}\right)^2\right]\right\}(1-(z^+)^2) \\ (f^+(x^+) \leqslant y^+ \leqslant 1). \end{cases} \tag{26}$$

The coefficients $a_3(x^+)$ and $b_3(x^+)$ are then obtained using the momentum equations (20) and (21). According to equation (21), $\partial p_v^+/\partial x^+$ must be independent of y^+. Using the polynomial velocity profile (26), equation (21) is satisfied relatively accurately by requiring:

$$\left.\frac{\partial p_v^+}{\partial x^+}\right|_{y^+=0} = \left.\frac{\partial p_v^+}{\partial x^+}\right|_{y^+=1} = \frac{\partial \bar{p}_v^+}{\partial x^+} \tag{27}$$

where the derivatives are determined with the help of equations (20), (22) and (26) and the bar denotes the average

$$\bar{p}_v^+ = \frac{1}{2}\int_0^1 \int_{-1}^1 p_v^+ \, dy^+ \, dz^+.$$

After a transformation we obtain the following equations for $a_3(x^+)$ and $b_3(x^+)$:

$$\frac{da_3}{dx^+} = \frac{-1}{(2A_1(x^+)a_3 + A_2(x^+))U_v^+(x^+)} \times \left\{\frac{5}{4Re_h}\left[\frac{a_3+2}{f^+(x^+)} + \frac{b_3+2}{1-f^+(x^+)} + \frac{\alpha^2}{4}(a_3 f^+(x^+) + b_3(1-f^+(x^+))+8)\right] + \frac{5}{4(f^+(x^+))^2} \times \left[\left(v_2^+ f^+(x^+) - \frac{4}{Re_h}\right)a_3 + 2\left(v_2^+ f^+(x^+) - \frac{1}{Re_h}\right)\right] + U_v^+(x^+)\left(a_3^2\frac{dA_1}{dx^+} + a_3\frac{dA_2}{dx^+} + \frac{dA_3}{dx^+}\right) + 2(A_1(x^+)a_3^2 + A_2(x^+)a_3 + A_3(x^+))\frac{dU_v^+(x^+)}{dx^+}\right\} \tag{28}$$

and

$$b_3(x^+) = B_1(x^+)a_3(x^+) + B_2(x^+) \tag{29}$$

where

$$A_1(x^+) = [f^+(x^+) + B_1^2(x^+)(1-f^+(x^+))]/105 \tag{30}$$

$$A_2(x^+) = \{4B_1(x^+)B_2(x^+)(1-f^+(x^+)) + 21[f^+(x^+) + B_1(x^+)(1-f^+(x^+))]\}/210 \tag{31}$$

$$A_3(x^+) = [B_2(x^+)(2B_2(x^+)+21)(1-f^+(x^+)) + 112]/210 \tag{32}$$

$$B_1(x^+) = \frac{\left(v_2^+ f^+(x^+) - \frac{4}{Re_h}\right)\Big/(f^+(x^+))^2}{\left[D_2(1-f^+(x^+)) - \frac{4}{Re_h}\right]\Big/(1-f^+(x^+))^2} \tag{33}$$

$$B_2(x^+) = \frac{2\left(v_2^+ f^+(x^+) - \frac{1}{Re_h}\right)\Big/(f^+(x^+))^2 - 2\left[D_2(1-f^+(x^+)) - \frac{1}{Re_h}\right]\Big/(1-f^+(x^+))^2}{\left[D_2(1-f^+(x^+)) - \frac{4}{Re_h}\right]\Big/(1-f^+(x^+))^2} \tag{34}$$

$$D_2 = \begin{cases} -1, & 0 \leqslant x^+ \leqslant \varphi \\ v_2^+, & \varphi \leqslant x^+ \leqslant 1 \end{cases}. \tag{35}$$

The maximum vapor velocity $U_v^+(x^+)$ is determined by integrating the continuity equation (16). Utilizing the velocity profile given by equation (26) and the boundary conditions (23), integration of the continuity equation (16) with respect to y^+ from 0 to 1 and z^+ from -1 to 1 yields:

$$U_v^+(x^+) = \begin{cases} \dfrac{18(1-v_2^+)}{[a_3(x^+)f^+(x^+) + b_3(x^+)(1-f^+(x^+))+8]}x^+ & 0 \leqslant x^+ \leqslant \varphi \\ \dfrac{36v_2^+}{[a_3(x^+)f^+(x^+) + b_3(x^+)(1-f^+(x^+))+8]}(1-x^+) & \varphi \leqslant x^+ \leqslant 1. \end{cases} \tag{36}$$

The location of maximum vapor velocity, $f^+(x^+)$, is determined by integrating the x^+-momentum equation (20) with respect to y^+ from 0 to $f^+(x^+)$ and with respect to z^+ from -1 to 1. Integration of the momentum equation (20) using the velocity profile (26) and boundary conditions (23) results in the following expression for the rate of change of $f^+(x^+)$:

$$\frac{df^+(x^+)}{dx^+} = \frac{-1}{4a_3^2(x^+) + 7a_3(x^+) - 56} \times \left\{\left[(8a_3(x^+)+7)\frac{da_3(x^+)}{dx^+} + \frac{(8a_3^2(x^+) + 49a_3(x^+) + 168)}{U_v^+(x^+)}\frac{dU_v^+(x^+)}{dx^+} + \frac{525\alpha^2}{4U_v^+(x^+)}\frac{a_3(x^+)+8}{Re_h} + \frac{1575}{2(U_v^+(x^+))^2}\frac{dp_v^+}{dx^+}\right] - \frac{525}{U_v^+(x^+)f^+(x^+)}\left(v_2^+ f^+(x^+) - \frac{a_3(x^+)+2}{Re_h}\right)\right\}. \tag{37}$$

The vapor pressure distribution is obtained by integrating the x^+-momentum equation (20) over the entire transverse section. Utilizing the derived velocity profile given in equation (26) and the boundary conditions given in equation (23), integration of the momentum equation (20) with respect to y^+ from 0 to 1 and with respect to z^+ from -1 to 1 yields:

$$\frac{dp_v^+}{dx^+} = -\frac{8}{15}\frac{d}{dx^+}\{(U_v^+(x^+))^2[(a_3^2(x^+)/105 + a_3(x^+)/10 + 8/15)f^+(x^+) + (b_3^2(x^+)/105 + b_3(x^+)/10 + 8/15)(1-f^+(x^+))]\} - \frac{2U_v^+(x^+)}{3Re_h}\left\{\left(\frac{a_3(x^+)+2}{f^+(x^+)} + \frac{b_3(x^+)+2}{1-f^+(x^+)}\right) + \frac{\alpha^2}{4}[(a_3(x^+)+8)f^+(x^+) + (b_3(x^+)+8)(1-f^+(x^+))]\right\}. \tag{38}$$

The set of differential equations (28), (37) and (38), is readily integrated simultaneously by using a fourth-order Runge–Kutta scheme.

Liquid flow

The governing equations (5)–(12) are non-dimensionalized using:

$$x^+ = \frac{x}{L},\quad y^+ = \frac{y}{h},\quad z^+ = \frac{z}{W/2},$$

$$u_{l,i}^+ = \frac{u_{l,i}}{u_l},\quad v_{l,i}^+ = \frac{v_{l,i}}{v_l},$$

$$w_{l,i}^+ = \frac{w_{l,i}}{w_l},\quad p_{l,i}^+ = \frac{p_{l,i}}{\rho_v u_l^2}. \tag{39}$$

This results in:

$$\frac{\partial u_{l,i}^+}{\partial x^+} + \frac{\partial v_{l,i}^+}{\partial y^+} + \frac{\partial w_{l,i}^+}{\partial z^+} = 0 \tag{40}$$

$$\frac{\partial p_{l,i}^+}{\partial x^+} = -\frac{1}{Re_h}\frac{\mu^+}{K_w^+}u_{l,i}^+ - \frac{\rho^+ F\varepsilon_w\beta}{(K_w^+)^{1/2}}|u_{l,i}^+|u_{l,i}^+ + \frac{1}{Re_h}\frac{\mu^+}{\varepsilon_w}\left(\frac{\partial^2 u_{l,i}^+}{\partial (y^+)^2} + \frac{1}{\alpha^2}\frac{\partial^2 u_{l,i}^+}{\partial (z^+)^2}\right) \tag{41}$$

$$Q^+(x^+) = \int_{-h_w^+}^{0}[w_{l,b}^+(x^+,y^+,1) - w_{l,b}^+(x^+,y^+,-1)]\,dy^+ = -\int_{1}^{1+h_w^+}[w_{l,t}^+(x^+,y^+,1) - w_{l,t}^+(x^+,y^+,-1)]\,dy^+ \tag{42}$$

$$Q^+(x^+) = -\frac{\beta^2 Re_h}{\alpha}\frac{K_{vw}^+ h_{vw}^+}{\mu^+}(p_{l,t}^+ - p_{l,b}^+ + \Delta p_g^+) \tag{43}$$

where

$$i = \begin{cases} t & \text{for the top liquid–wick region} \\ b & \text{for the bottom liquid–wick region} \end{cases}$$

and

$$\rho^+ = \frac{\rho_l}{\rho_v},\quad \mu^+ = \frac{\mu_l}{\mu_v},\quad K_w^+ = \frac{K_w}{h^2},$$

$$K_{vw}^+ = \frac{K_{vw}}{h^2},\quad h_{vw}^+ = \frac{h_{vw}}{h},$$

$$\beta = \frac{L}{h},\quad \Delta p_g^+ = \frac{\rho_l g h}{\rho_v u_l^2}. \tag{44}$$

It is noted that the axial shear stress is negligible compared to the transverse shear stress. The boundary conditions in dimensionless form reduce to:

$$u_{l,t}^+(0,y^+,z^+) = u_{l,b}^+(0,y^+,z^+) = u_{l,t}^+(1,y^+,z^+) = u_{l,b}^+(1,y^+,z^+) = 0$$

$$u_{l,t}^+(x^+,1+h_w^+,z^+) = v_{l,t}^+(x^+,1+h_w^+,z^+) = w_{l,t}^+(x^+,1+h_w^+,z^+) = 0$$

$$u_{l,t}^+(x^+,1,z^+) = w_{l,t}^+(x^+,1,z^+) = 0,$$

$$v_{l,t}^+(x^+,1,z^+) = \begin{cases} -\dfrac{1}{\rho^+} & 0 \leqslant x^+ \leqslant \varphi \\ \dfrac{v_2^+}{\rho^+} & \varphi \leqslant x^+ \leqslant 1 \end{cases}$$

$$u_{l,b}^+(x^+,0,z^+) = w_{l,b}^+(x^+,0,z^+) = 0,$$

$$v_{l,b}^+(x^+,0,z^+) = -\frac{v_2^+}{\rho^+}$$

$$u_{l,b}^+(x^+,-h_w^+,z^+) = v_{l,b}^+(x^+,-h_w^+,z^+) = w_{l,b}^+(x^+,-h_w^+,z^+) = 0$$

$$u_{l,t}^+(x^+,y^+,1) = u_{l,b}^+(x^+,y^+,1) = u_{l,t}^+(x^+,y^+,-1) = u_{l,b}^+(x^+,y^+,-1) = 0$$

$$p_{l,b}^+(1,y^+,z^+) = p_v^+(1,y^+,z^+). \tag{45}$$

For liquid flow within the top and bottom wicks, the liquid velocity component in the x^+-direction can be assumed as:

$$u_{l,t}^+(x^+,y^+,z^+) = u_{l,t}^+(x^+,y^+)(c_0 + c_1 z^+ + c_2 (z^+)^2) \tag{46}$$

$$u_{l,b}^+(x^+,y^+,z^+) = u_{l,b}^+(x^+,y^+)(c_0 + c_1 z^+ + c_2 (z^+)^2). \tag{47}$$

Applying the boundary conditions given by equation (45) to equations (46) and (47) yields:

$$u_{l,t}^+(x^+,y^+,z^+) = u_{l,t}^+(x^+,y^+)(1-(z^+)^2) \tag{48}$$

$$u_{l,b}^+(x^+,y^+,z^+) = u_{l,b}^+(x^+,y^+)(1-(z^+)^2). \tag{49}$$

Vafai and Thiyagaraja [12] have shown that the momentum boundary layer thickness at the interface between a porous medium and a fluid or an impermeable medium is of the order of $(K/\varepsilon)^{1/2}$. According to their investigation of the interface interactions in a saturated porous medium, the liquid velocity profile in the top and bottom wicks can be represented by three parts: an inner solution for the interface zone between the liquid–wick and the vapor phase, an outer solution for the main wick region and an inner solution for the interface zone between the liquid–wick and the heat pipe wall. Based on the matched asymptotic solution of Vafai and Thiyagaraja [12], by applying the boundary conditions given by equation (45) and noting that the thickness of the interface regions is much smaller than $h_w/2$ for the heat pipe under study, the following velocity profile is obtained for the liquid flow within the bottom wick ($-h_w^+ \leqslant y^+ \leqslant 0$):

$$u_{l,b}^{+}(x^{+},y^{+}) = \begin{cases} U_{l,b}^{+}(x^{+})\left[1-\exp\left(\dfrac{y^{+}}{Da_{w}^{1/2}}\right)\right] \\ \quad -\dfrac{h_{w}^{+}}{2} \leqslant y^{+} \leqslant 0 \\ U_{l,b}^{+}(x^{+})\left[1-\exp\left(-\dfrac{y^{+}+h_{w}^{+}}{Da_{w}^{1/2}}\right)\right] \\ \quad -h_{w}^{+} \leqslant y^{+} \leqslant -\dfrac{h_{w}^{+}}{2} \end{cases} \quad (50)$$

and for the liquid flow within the top wick $(1 \leqslant y^{+} \leqslant 1+h_{w}^{+})$

$$u_{l,t}^{+}(x^{+},y^{+}) = \begin{cases} U_{l,t}^{+}(x^{+})\left[1-\exp\left(\dfrac{1-y^{+}}{Da_{w}^{1/2}}\right)\right] \\ \quad 1 \leqslant y^{+} \leqslant 1+\dfrac{h_{w}^{+}}{2} \\ U_{l,t}^{+}(x^{+})\left[1-\exp\left(-\dfrac{y^{+}-(1+h_{w}^{+})}{Da_{w}^{1/2}}\right)\right] \\ \quad 1+\dfrac{h_{w}^{+}}{2} \leqslant y^{+} \leqslant 1+h_{w}^{+} \end{cases} \quad (51)$$

where $U_{l,b}^{+}(x^{+})$ and $U_{l,t}^{+}(x^{+})$ denote the maximum liquid velocity on every transverse surface within the bottom and top wicks, respectively, and $Da_{w} = K_{w}^{+}/\varepsilon_{w}$ is the modified Darcy number of the top and bottom wicks.

The maximum liquid velocities $U_{l,b}^{+}(x^{+})$ and $U_{l,t}^{+}(x^{+})$ are determined by integrating the liquid continuity equations. For liquid flow within the bottom wick, integration of the liquid continuity equation (40) with respect to y^{+} from $-h_{w}^{+}$ to 0 and with respect to z^{+} from -1 to 1 results in the following expression for $U_{l,b}^{+}(x^{+})$:

$$U_{l,b}^{+}(x^{+}) = \frac{3}{2h_{w}^{+}}\left[\frac{v_{2}^{+}}{\rho^{+}}x^{+} + \frac{\beta^{2}Re_{h}}{2\alpha}\frac{K_{vw}^{+}h_{vw}^{+}}{\mu^{+}}\int_{0}^{x^{+}}(p_{l,t}^{+}-p_{l,b}^{+}+\Delta p_{g}^{+})\,dx^{+}\right]. \quad (52)$$

The liquid velocity profile given by equations (49) and (50), the boundary conditions given by (45) and equations (42) and (43) were utilized during this integration. For the liquid flow within the top wick, integration of the liquid continuity equation (40) with respect to y^{+} from 1 to $1+h_{w}^{+}$ and with respect to z^{+} from -1 to 1 results in the following expression for $U_{l,t}^{+}(x^{+})$:

$$U_{l,t}^{+}(x^{+}) = \begin{cases} -\dfrac{3}{2h_{w}^{+}}\left[\dfrac{1}{\rho^{+}}x^{+} + \dfrac{\beta^{2}Re_{h}}{2\alpha}\dfrac{K_{vw}^{+}h_{vw}^{+}}{\mu^{+}} \times \displaystyle\int_{0}^{x^{+}}(p_{l,t}^{+}-p_{l,b}^{+}+\Delta p_{g}^{+})\,dx^{+}\right] \\ \quad 0 \leqslant x^{+} \leqslant \varphi \\ \dfrac{3}{2h_{w}^{+}}\left[\dfrac{v_{2}^{+}}{\rho^{+}}(x^{+}-2) - \dfrac{\beta^{2}Re_{h}}{2\alpha}\dfrac{K_{vw}^{+}h_{vw}^{+}}{\mu^{+}} \times \displaystyle\int_{0}^{x^{+}}(p_{l,t}^{+}-p_{l,b}^{+}+\Delta p_{g}^{+})\,dx^{+}\right] \\ \quad \varphi \leqslant x^{+} \leqslant 1. \end{cases} \quad (53)$$

The liquid velocity profile given by equations (48) and (51), the boundary conditions given by (45), and equations (42) and (43) were utilized during the integration.

The liquid pressure distributions are obtained by integrating the generalized momentum equations (41) within the top and bottom wicks, respectively. For the liquid flow within the bottom wick, integrating equation (41) with velocity profile given by equations (49) and (50) and the boundary conditions given by equations (45) yields

$$\frac{dp_{l,b}^{+}}{dx^{+}} = -\frac{2}{3Re_{h}}\left(1+\frac{2Da_{w}^{1/2}}{h_{w}^{+}}+\frac{3Da_{w}}{\alpha^{2}}\right)\frac{\mu^{+}}{K_{w}^{+}}U_{l,b}^{+}(x^{+}) + \frac{8\beta}{15}\left(1-\frac{3Da_{w}^{1/2}}{h_{w}^{+}}\right)\frac{\rho^{+}F\varepsilon_{w}}{(K_{w}^{+})^{1/2}}(U_{l,b}^{+}(x^{+}))^{2}. \quad (54)$$

Similarly, integration of equation (41) with the velocity profile given by equations (48) and (51) and the boundary conditions given by equation (45) results in the following expression for the liquid pressure gradient within the top wick:

$$\frac{dp_{l,t}^{+}}{dx^{+}} = -\frac{2}{3Re_{h}}\left(1+\frac{2Da_{w}^{1/2}}{h_{w}^{+}}+\frac{3Da_{w}}{\alpha^{2}}\right)\frac{\mu^{+}}{K_{w}^{+}}U_{l,t}^{+}(x^{+}) + \frac{8\beta}{15}\left(1-\frac{3Da_{w}^{1/2}}{h_{w}^{+}}\right)\frac{\rho^{+}F\varepsilon_{w}}{(K_{w}^{+})^{1/2}}(U_{l,t}^{+}(x^{+}))^{2}. \quad (55)$$

The coupled equations (52)–(55) are solved numerically for the liquid velocity profiles and pressure distributions within the top and bottom wicks.

NUMERICAL SIMULATION OF THE VAPOR FLOW

The complete problem for the three-dimensional vapor flow within the flat plate heat pipe was also analyzed numerically in the present work. The full set of governing equations (1)–(4), along with boundary conditions given by equation (13), were solved over the entire vapor flow channel in order to allow all the features of the incompressible vapor flow to be taken

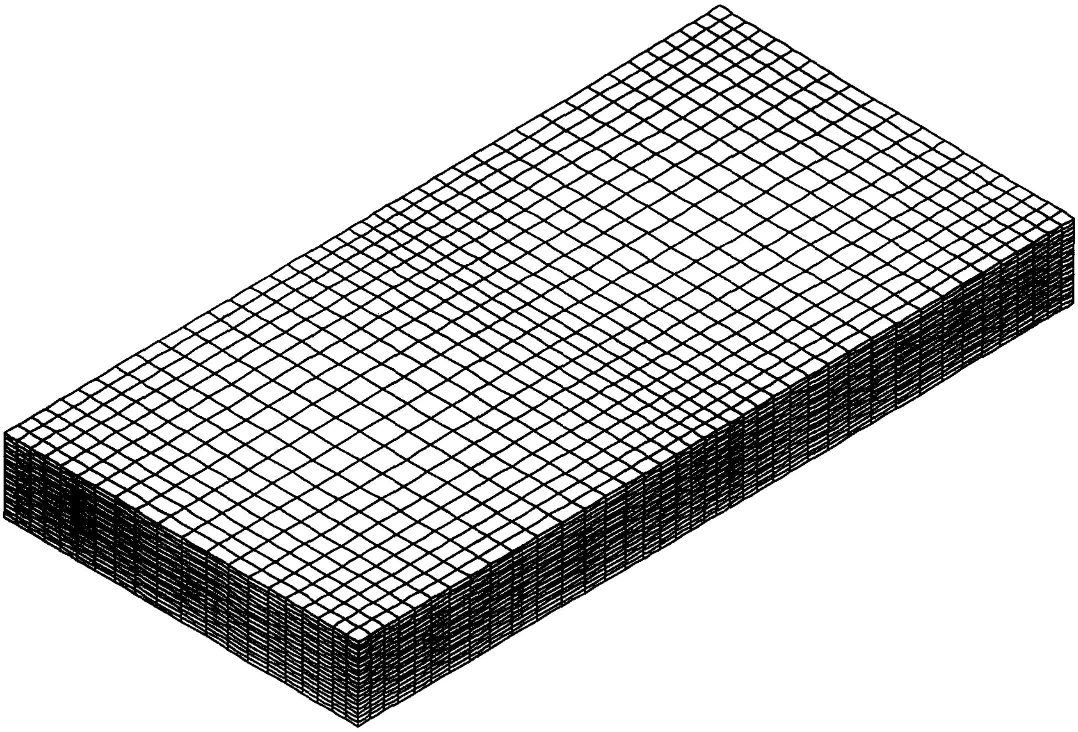

Fig. 2. Finite element mesh used for the numerical computations.

into account. The discretization of the governing equations (1)–(4) along with the boundary conditions was carried out by using a finite element formulation based on the Galerkin method of weighted residuals. The finite element mesh used in the present study is shown in Fig. 2. The 27-node quadratic elements were used for discretizing the computational domain, resulting in a triquadratic interpolation for the velocity. A trilinear interpolation was used for the pressure approximations. A variable mesh grading strategy was adopted to capture sharper gradients in the velocity and pressure at the liquid–vapor interfaces and the transition region from the evaporator section to the condenser section. To confirm the grid independence of the three-dimensional model, results were obtained by increasing the grid points from the $81 \times 41 \times 41$ mesh to a $121 \times 61 \times 61$ mesh. A comparison of magnitudes of the vapor velocity and pressure for various runs showed that these values change by less than 1%, thus indicating that the grid structure is sufficiently fine.

The discretization of the governing equations along with the boundary conditions results in a highly nonlinear, coupled system of algebraic equations. This system of equations was then solved by using an iterative solution scheme based on the segregated solution algorithm. Basically, this scheme involves decomposition of the entire system of equations into smaller subsystems. Each subsystem is then solved by using an iterative solver. Convergence was assumed to have been reached when the relative change in variables between consecutive iterations was less than 10^{-3}. The application of the Galerkin-based FEM is well-described by Taylor and Hood [13], and its application in the finite element program used in the present work is also well-documented [14]. In order to investigate the three-dimensional effects on the vapor flow, a two-dimensional analysis was also performed using the finite element method.

RESULTS AND DISCUSSION

The results presented here are based on a copper heat pipe with heavy water as the working fluid. It should be noted that the heat pipe material is chosen to be copper instead of aluminum (which is more compatible from the neutronic side), due to the compatibility of copper and heavy water. The respective dimensions of the heat pipe are chosen as: $L = 0.25$ m, $L_e = 0.125$ m, $h = 0.025$ m, $W = 0.125$ m and $h_w = h_{vw} = 0.0025$ m. The top, bottom and vertical wicks are sintered copper powder. The wick porosity and permeability for the top and bottom wicks were chosen as 0.9 and 1.5×10^{-9} m^2, respectively. The permeability of the vertical wicks was chosen as 2.1×10^{-10} m^2. The results in Figs 3–9 were obtained for the operating temperature of 80°C and for Re_h values of 25, 50, 75, 100, 150 and 200.

Figures 3 and 4 show the dimensionless vapor velocity profiles along the center plane ($z^+ = 0$) in the evaporator zone and condenser zone, respectively. Both numerical and analytical results show that the vapor velocity profiles are symmetrical about the $z^+ = 0$ plane, due to the symmetrical boundary con-

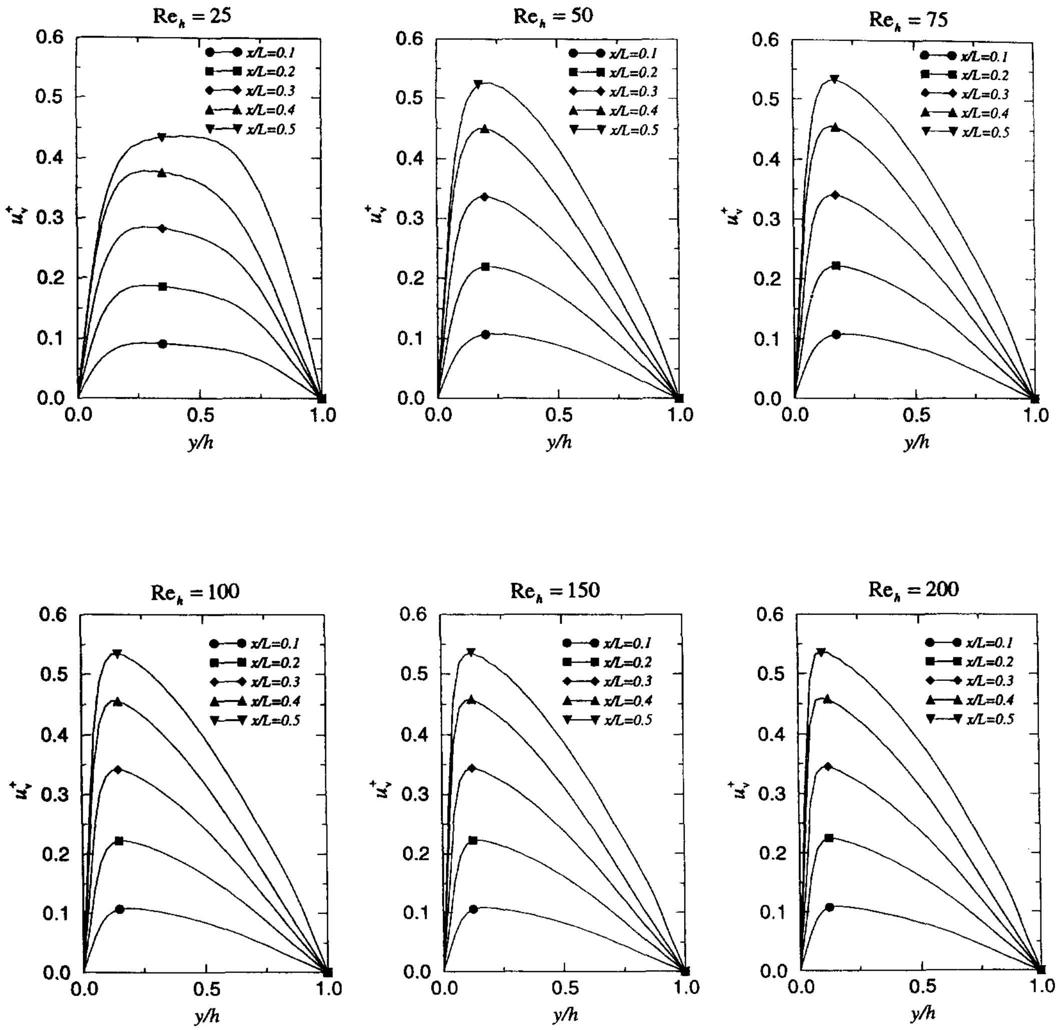

Fig. 3. Dimensionless longitudinal velocity profiles along the center plane ($z^+ = 0$) of the evaporator section.

ditions at the vertical wicks. However, the vapor velocity profiles are asymmetrical in the x^+–y^+ plane, due to the asymmetrical heat and cooling conditions. As can be seen from Figs 3 and 4, the velocity maxima are shifted towards the bottom wick in the evaporator section, due to injection from the top wick and suction from the bottom wick. With increasing Re_h values, shifting is more prominent, giving an increase in the wall shear stress at the bottom wall and a decrease at the top wall. Within the condenser section, the shifted velocity maxima moves back towards the center line ($y^+ = 1/2$) due to the symmetrical cooling condition over the condenser zone.

Vapor accelerates in the evaporator section and decelerates in the condenser section, due to the vapor injection and suction over the corresponding regions. For Re_h larger than 75, vapor flow separation takes place, which leads to a region of reversed flow near the top entrance of the condenser section. As can be seen in Fig. 4, flow separation always starts shortly after the vapor flow enters the condenser zone and results in a recirculating flow cell downstream. As the Re_h value increases, the separation point with zero wall shear stress moves upstream towards the condenser entrance and the recirculation expands towards the end of the condenser section. At $Re_h = 200$, the separation point is found right at the starting point of the condenser zone and flow reversal is present at all locations of the condenser zone. It is worth noting that no flow reversal is found in the evaporator zone. This is consistent with conventional symmetrical heat pipes.

Figure 5 compares the analytical u velocity profiles along the heat pipe at the center plane ($z^+ = 0$) with the numerical prediction for Re_h values of 25, 50, 75, 100, 150 and 200. Agreement between the analytical and the numerical predictions is very good over the entire vapor flow domain. This indicates that the analytical model can accurately describe vapor velocity profiles under conditions including strong flow reversal, while saving tremendous computational time as compared to that of a numerical simulation. Fur-

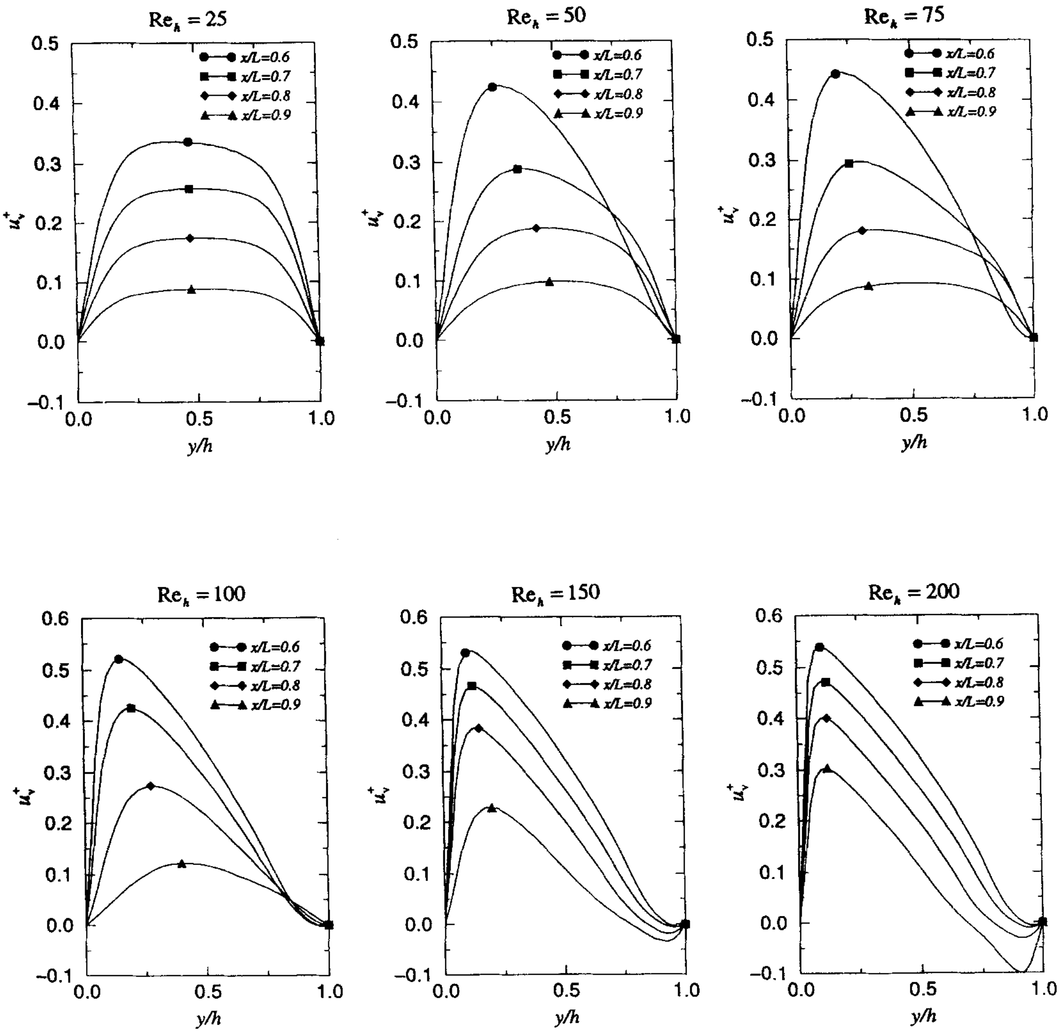

Fig. 4. Dimensionless longitudinal velocity profiles along the center plane ($z^+ = 0$) of the condenser section.

thermore, the analytical solution also reveals qualitative functional dependency on various physical parameters involved in the flat plate heat pipe.

Figure 6 shows the vapor pressure distributions along the heat pipe. Our numerical results show that the transverse pressure differences in the y^+-direction are negligibly small. Therefore, a single graph was used to represent the pressure distribution along the heat pipe for all y-values. This is consistent with the two-dimensional analysis by Ooijen and Hoogendoorn [3]. As can be seen in Fig. 6, the vapor pressure decreases in the evaporator zone due to friction and acceleration of the vapor flow caused by mass injection from the top wick, while the vapor pressure increases in the condenser zone owing to the deceleration of the vapor flow by mass suction. It was found that for $Re_h \leqslant 10$, the frictional effect dominates and the vapor pressure decreases over the condenser zone. For higher Re_h values, the inertial effect becomes dominant and the pressure build up occurs in the condenser zone. Figure 6 also shows the comparison of the analytical vapor pressure distributions along the heat pipe with the numerical prediction for Re_h values of 25, 50, 75, 100, 150 and 200. The analytical results for all Re_h values shown agree very well with the numerical predictions over the evaporator zone and quite well in the condenser zone. Despite a relatively small discrepancy between the analytical predictions and the numerical calculations in the condenser zone, the analytical and numerical predictions of the total pressure drops along the heat pipe agree with each other very well.

It should be noted that this is the first time that a three-dimensional numerical simulation of the vapor flow in a flat plate heat pipe has been presented. For a flat plate heat pipe with several vapor flow channels divided by vertical wicks, three-dimensional effects may become a critical factor in modeling the vapor flow. Figure 7 shows the comparison of the two-dimensional model predictions of vapor pressure distributions with the three-dimensional model predictions. As can be seen in Fig. 7, the two-dimensional model, which neglects the viscous shearing effects due to the side walls, results in smaller total vapor-pressure

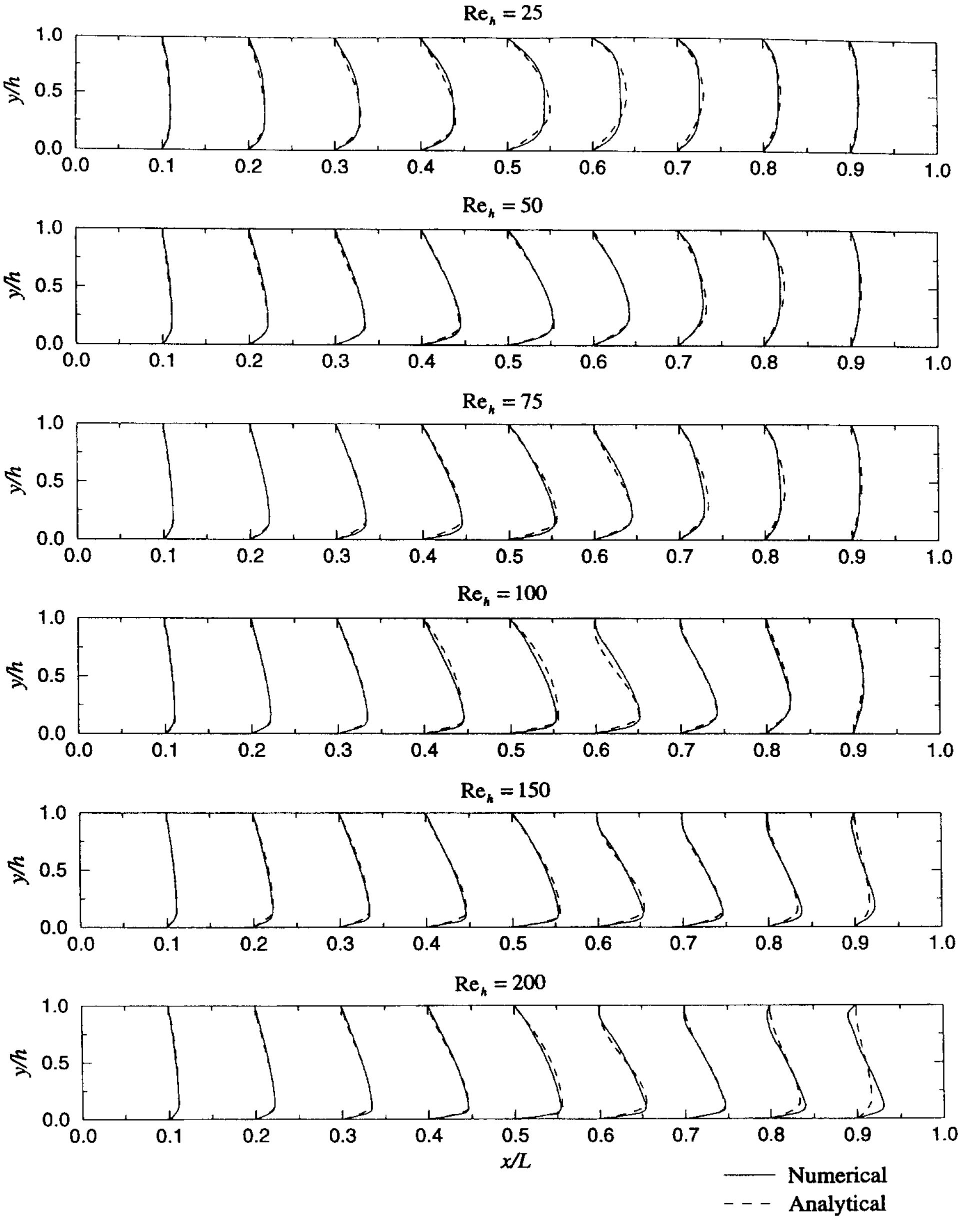

Fig. 5. Comparison of the numerical and analytical velocity profiles along the center plane ($z^+ = 0$) for $Re_h = 25, 50, 75, 100, 150$ and 200.

drops along the heat pipe. The smaller the ratio of the vapor-channel width to height, W/h, the larger the error caused by using the two-dimensional model. This is expected as the viscous shear loss due to the side walls increases with a decrease of this ratio. Our computations revealed that a three-dimensional model is necessary for $W/h \leqslant 2.5$. However, the use of a three-dimensional model substantially increases the computational time. Our results also show that the error caused by using the two-dimensional model decreases with an increase in the injection Reynolds number, Re_h. This is due to the inertial effect being more dominant than viscous effect at larger Re_h values.

The analytical results for the maximum liquid velocities are shown in Fig. 8. The negative velocity value denotes that the flow is along the negative x^+-direction. The liquid in the top wick accelerates in the condenser zone and decelerates in the evaporator zone due to the condensation and evaporation in the corresponding regions. The liquid in the bottom wick accelerates in the condenser zone until part of it is transferred to the top wick through the vertical wicks. At the condenser region close to the end of the heat

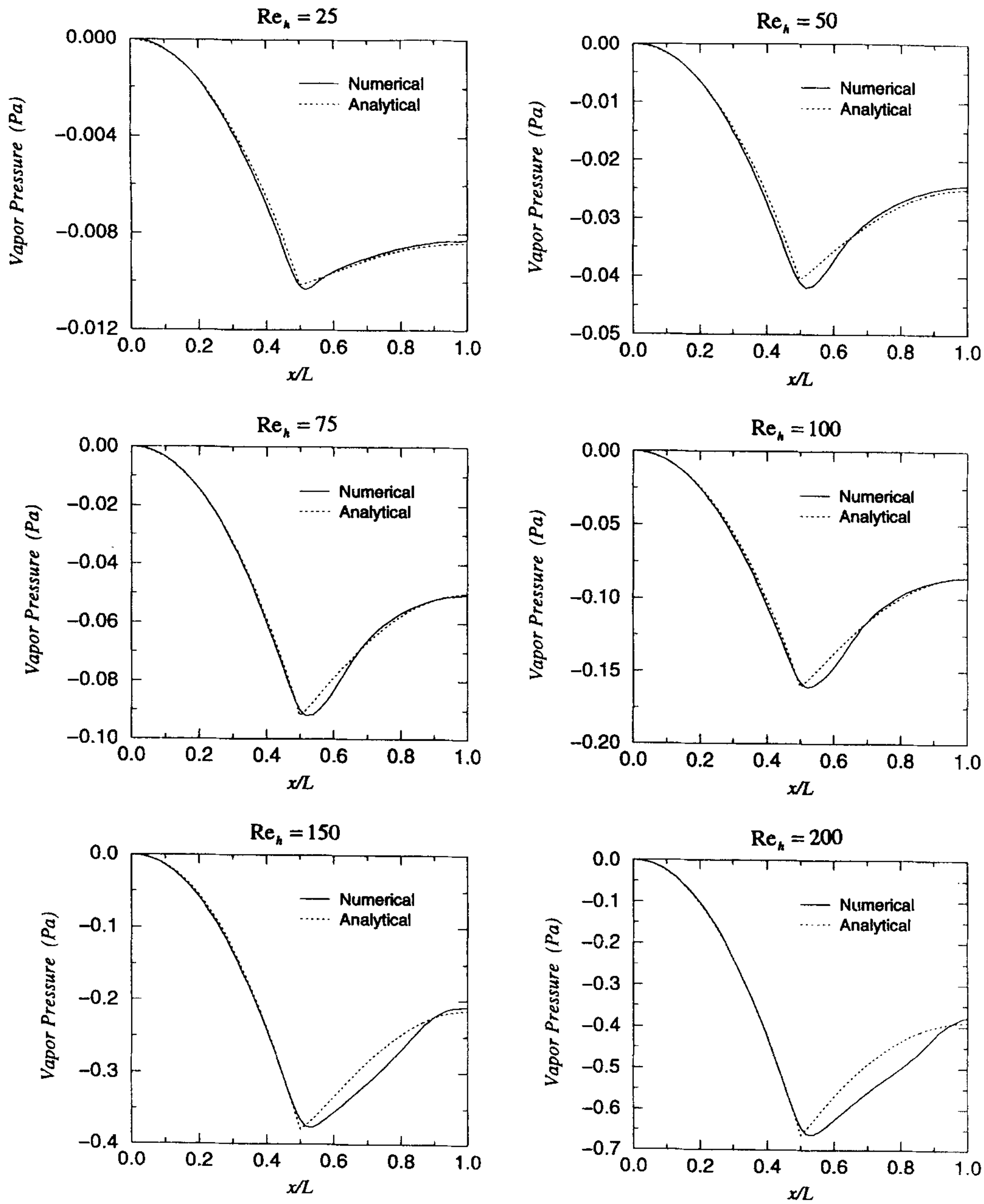

Fig. 6. Comparison of the numerical and analytical pressure distributions along the heat pipe for various injection Reynolds numbers.

pipe ($x^+ = 1$), there is no liquid exchange through the vertical wicks due to symmetrical cooling conditions and the liquid flow rates in the top and bottom wicks are the same. Starting at a certain location (around $x^+ = 0.7$), part of the liquid in the bottom wick is transferred to the top wick through the vertical wicks and leads to a larger liquid flow rate in the top wick.

Figure 9 shows the analytical results of liquid pressure distributions along the heat pipe. As expected, the liquid pressure in the top wick is always smaller than that in the bottom wick. In the region where no mass exchange through the vertical wicks occurs, the difference between the liquid pressures in the top and bottom wicks is only caused by gravity and is constant. In the region where the mass exchange through the vertical wicks occurs, this difference is caused by gravity and the frictional resistance for the liquid flow in the vertical wicks.

CONCLUSIONS

A comprehensive pseudo-three-dimensional analytical model has been developed for the vapor and liquid flow in an asymmetrical flat plate heat pipe under conditions including strong flow reversal. The

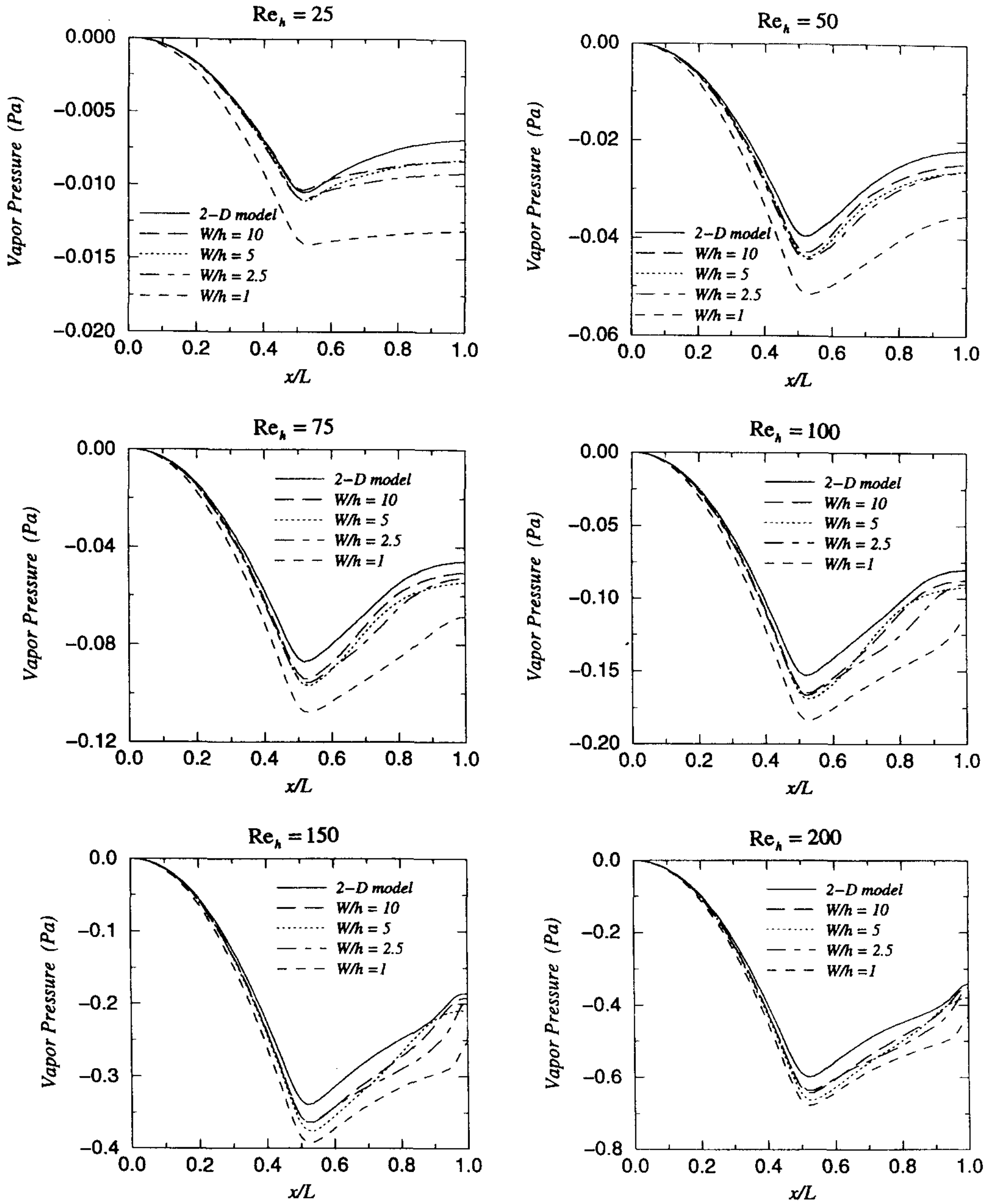

Fig. 7. Three-dimensional effects on the pressure distributions along the heat pipe for various injection Reynolds numbers.

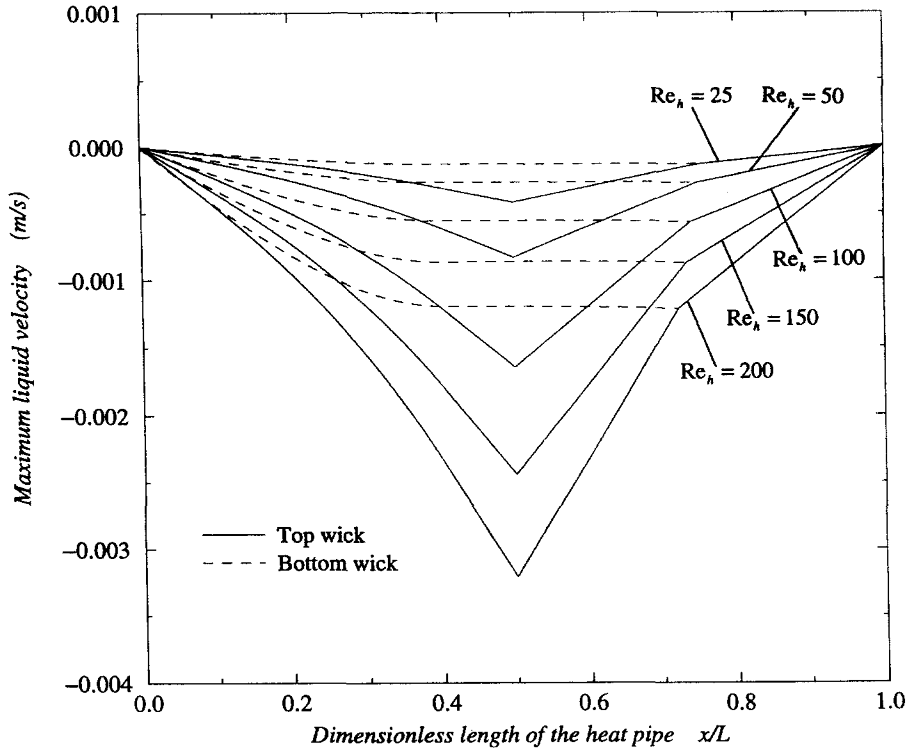

Fig. 8. Variations of the maximum liquid velocities along the heat pipe for various injection Reynolds numbers.

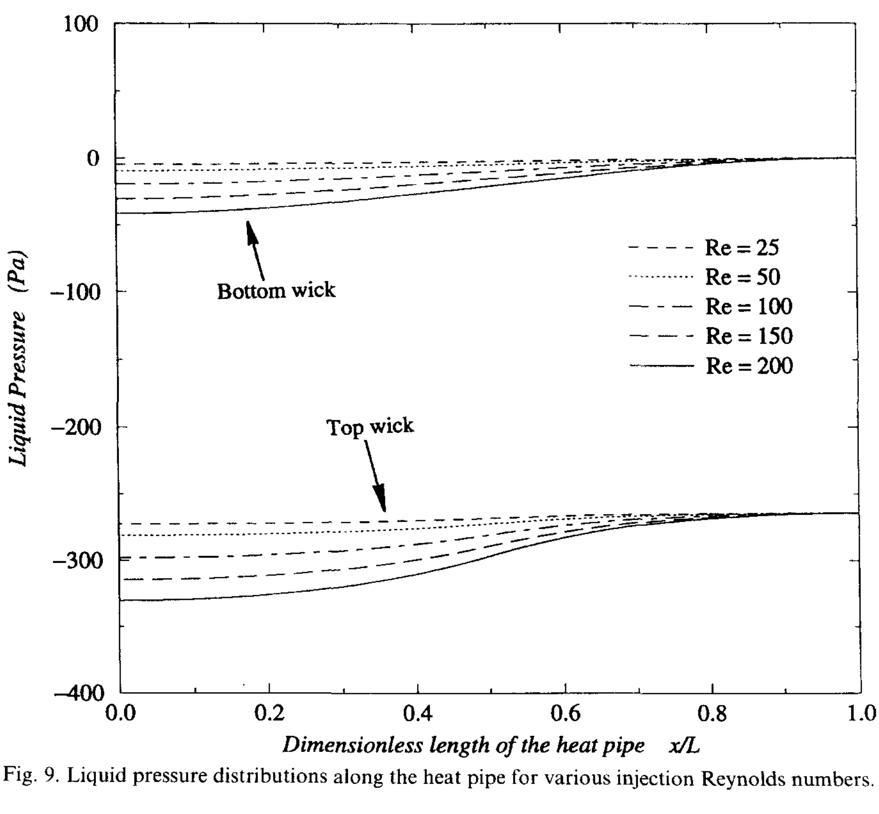

Fig. 9. Liquid pressure distributions along the heat pipe for various injection Reynolds numbers.

gravitational effects and the effects of non-Darcian transport through the porous wicks were included in the model. A three-dimensional numerical analysis of the vapor flow in the flat plate heat pipe has also been carried out for the first time. Both the analytical and the numerical results reveal that the vapor velocity profiles are nonsimilar and asymmetrical for the injection Reynolds number in the range of $25 \leqslant Re_h \leqslant 200$. Vapor flow reversal was observed along the top condenser region for $Re_h \geqslant 75$. It was observed that the transverse pressure variations are relatively small and can be neglected. It was established that a three-dimensional model is necessary for the prediction of the total vapor pressure drop within the heat pipe for $W/h \leqslant 2.5$. The analytical solutions were shown to agree very well with the numerical results. While drastically cutting down on the computational time and aiding in understanding the physical phenomena occurring in the problem, the analytical model is very useful for engineering design and optimization purposes by providing an accurate prediction method for the flat plate heat pipe operation and showing qualitatively and quantitatively the effects of various physical parameters.

Acknowledgement—The grant (DE-F602-93ER61612) by the Department of Energy is acknowledged and greatly appreciated.

REFERENCES

1. Dunn, P. D. and Reay, D. A., *Heat Pipes*, 3rd edn. Pergamon Press, New York, 1982.
2. Thomson, M., Ruel, C. and Donato, M., Characterization of a flat plate heat pipe for electronic cooling in a space environment. *1989 National Heat Transfer Conference*, Philadelphia, PA HTD-Vol. 111, 1989, pp. 59–65.
3. Ooijen, H. and Hoogendoorn, C. J., Vapor flow calculations in a flat-plate heat pipe. *AIAA Journal*, 1979, **17,** 1251–1259.
4. Vafai, K. and Wang, W., Analysis of flow and heat transfer characteristics of an asymmetrical flat plate heat pipe. *International Journal of Heat and Mass Transfer*, 1992, **35,** 2087–2099.
5. North, M. T. and Avedisian, C. T., Heat pipe for cooling high flux/high power semiconductor chips. *Journal of Electronic Packaging*, 1993, **115,** 112–117.
6. Vafai, K., Zhu, N., and Wang, W., Analysis of asymmetrical disk-shaped and flat plate heat pipes. *ASME Journal of Heat Transfer*, 1995, **117,** 209–218.
7. Zhu, N. and Vafai, K., The effects of liquid–vapor coupling and non-Darcian transport on asymmetrical disk-shaped heat pipes. *International Journal of Heat and Mass Transfer*, 1996, **39,** 2095–2113.
8. Zhu, N. and Vafai, K., Numerical and analytical investigation of vapor flow in a disk-shaped heat pipe incorporating secondary flow. *International Journal of Heat and Mass Transfer*, 1997, **40,** 2887–2900.
9. Vafai, K. and Tien, C. L., Boundary and inertia effects on flow and heat transfer in porous media. *International Journal of Heat and Mass Transfer*, 1981, **24,** 195–203.
10. Vafai, K., Convective flow and heat transfer in variable porosity media. *Journal of Fluid Mechanics*, 1984, **147,** 233–259.
11. Busse, C. A. and Prenger, F. C., Numerical analysis of the vapor flow in cylindrical heat pipes. *Proceedings of the 5th International Heat Pipe Conference*, Part I, JATEC, Tokyo, Japan, 1984, pp. 214–219.
12. Vafai, K. and Thiyagaraja, R., Analysis of flow and heat transfer at the interface region of a porous medium. *International Journal of Heat and Mass Transfer*, 1987, **30,** 1391–1405.
13. Taylor, C. and Hood, P., A numerical solution of the Navier–Stokes equations using the finite-element technique. *Computational Fluids*, 1973, **1**, 73–89.
14. *FIDAP Theoretical Manual*, Fluid Dynamics International, Evaston, IL, 1993.